The **annual** evolution of **ice-ocean interaction** beneath landfast ice in Prydz Bay, East Antarctica

Haihan Hu[1], Jiechen Zhao[2, 3*], Petra Heil[4], Jingkai Ma[5], Fengming Hui[1*], Xiao Cheng[1]

[1]School of Geospatial Engineering and Science, Sun Yat-sen University, and Southern Marine Science and Engineering Guangdong Laboratory (Zhuhai), Zhuhai 519082, China;

[2]Qingdao Innovation and Development Base (Centre) of Harbin Engineering University, Qingdao, 266500, China;

[3]College of Underwater Acoustic Engineering, Harbin Engineering University, Harbin 150001, China;

[4]Australia Antarctic Division & Australian Antarctic Programmer Partnership, Private Bag 80, Hobart TAS 7001, Australia;

[5]Key Laboratory of Research on Marine Hazards Forecasting, National Marine Environmental Forecasting Centre, Beijing 100081, China.

Correspondence to: Jiechen Zhao (zhaojiechen@hrbeu.edu.cn) and Fengming Hui (huifm@mail.sysu.edu.cn)

Abstract: The ice–ocean interaction is one of the main drivers of sea ice mass balance in the Polar Regions. To investigate the oceanic contribution to the landfast ice evolution, an integrated ocean observation system, including Acoustic Doppler Velocimeter (ADV), Conductivity–Temperature–Depth (CTD) sensors, and Sea Ice Mass Balance Array (SIMBA), was deployed at the landfast ice near Chinese Zhongshan Station in Prydz Bay, East Antarctica, from April to November 2021. CTD recorded ocean temperature and salinity. Ocean temperature experienced a jump increase in late April, from -1.6°C to the maximum of -1.3°C, then gradually decreased to -1.75°C in May and maintained until November. Ocean salinity and density experienced a similar increase trend during April and May, with mean rates of 0.04 psu day^{-1} and 0.03 kg m^{-3} day^{-1}, respectively, related to the strong salt rejection caused by landfast ice freezing. The ocean current observed by ADV showed an annual mean of 9.5±3.9 cm s^{-1} for horizontal velocity and 0.2±0.8 cm s^{-1} for vertical velocity. The domain current direction was NWW (-60°)–NEE (60°) and the domain velocity (79%) was 5–15 cm s^{-1}. Oceanic heat flux (F_w) estimated by the residual method, indicated a peak of 41.33±9.81 W m^{-2} in April, and then gradually decrease to a stable level of 7.77±2.99 W m^{-2} from June to October. The F_w calculated by three different bulk parameterizations showed similar trends with different magnitudes, due to the uncertainties of the empirical friction velocity. The spectral analysis suggested that all the observed ocean variables showed a typical period of 0.5 days, indicating the strong diurnal influence of local tide oscillation. The large-scale sea ice distribution and ocean circulation contributed to the seasonal variation of ocean variables, revealing the important relationship between large-scale and local phenomena. The high frequency and long-term observations of oceanic variables allow us to deeply investigate their diurnal and seasonal variation and evaluate their influences on sea ice evolution.

1 Introduction

In recent years, global warming has been becoming more and more significant, especially in the high Arctic (Manabe and Stouffer, 1980; Screen and Simmonds, 2010; Clem et al., 2020). The Antarctic sea ice plays a critical role in driving and

modulating global climate change, and local marine and ecosystem systems (Massom and Stammerjohn, 2010). However, in contrast to the quick decline of sea ice extent in the Arctic, the Antarctic experienced a slight increase since the late 1970s (Comiso et al., 2008; Liu and Curry, 2010), with an extended peak of 20 million km² observed in 2014, and then exhibited a decreasing trend in summer minima and winter maxima, until reached a new low in 2021/22 (Parkinson and DiGirolamo, 2021; Raphael and Handcock, 2022; Wang et al., 2022).

Landfast ice commonly exists along the Antarctic coast, usually attached to the shorelines, ice shelves, glacier tongues, grounded icebergs, or shoals (Massom et al., 2001; Li et al., 2020). In contrast to pack ice floes, landfast ice generally shows a longer annual duration and a larger thickness, and their width can reach tens to hundreds of kilometres from the shore (Fraser et al., 2021). In winter of the Southern Hemisphere, landfast ice accounts for about 3–4% of the total sea ice area (Li et al., 2020), and a larger percentage of 14–20% of the total sea ice volume (Fedotov et al., 2013). In particular, the proportion of landfast ice off East Antarctica is larger than other Antarctic regions (Giles et al., 2008; Li et al., 2020). As a natural boundary between the ocean and atmosphere, landfast ice strongly influences the air–ocean interaction and the heat and momentum exchange (Maykut and Untersteiner, 1971; Heil et al., 1996; Heil, 2006). The existence of landfast ice provides an efficient barrier to glaciers and ice sheets, preventing them calve and vanish into the Southern Ocean (Massom and Stammerjohn, 2010; Miles et al., 2017).

The growth of landfast ice is mainly attributed to the thermodynamic processes. Oceanic heat flux plays a critical role in the ice mass balance and influences the annual landfast ice growth (Parkinson and Washington, 1979). However, oceanic heat flux is hard to observe directly, usually estimated by measuring the ice temperature and thickness (McPhee and Untersteiner, 1982). Heil et al. (1996) estimated the annual oceanic heat flux to be 5–12 W m^{-2} based on ice observations in Australia's Antarctica Mawson Station. Lei et al. (2010) studied the seasonal variation of landfast ice in Prydz Bay in 2006 and obtained an oceanic heat flux of 11.8±3.5 W m^{-2} in April and an annual minimum of 1.9±2.4 W m^{-2} in September, based on the residual method. Yang et al. (2016) analysed the oceanic heat flux in Prydz Bay by the HIGHTSI (High-resolution thermodynamic snow and ice) model (Launiainen and Cheng, 1998; Vihma, 2002; Cheng et al., 2006) and concluded that it gradually decreased from 25 W m^{-2} to 5 W m^{-2} in winter. Zhao et al. (2019) estimated the oceanic heat flux by the residual method and found that the monthly oceanic heat flux in 2012 was 30 W m^{-2} in March–May, reduced to 10 W m^{-2} during July–October, and increased back to 15 W m^{-2} in November. In terms of the evolution mechanism of oceanic heat flux, Allison (1981) found that oceanic heat flux under landfast ice near Mawson Station showed two peaks throughout the season, due to the influence of thermohaline convection caused by salt rejection, and seasonal variation of large-scale meridional thermal advection in the Southern Ocean. McPhee et al. (1996) found that oceanic heat flux changed on the sub-diurnal scale due to the sub-glacial cold and warm currents.

The direct observation of high-frequency ocean temperature, salinity, and velocity beneath landfast ice near the Chinese Antarctic Zhongshan Station is important to fill the data gap in the ice–ocean model parameterization, and to exactly understand how oceanic heat flux affects the sea ice growth in Prydz Bay in a diurnal and seasonal scale. In this study, a set of ice–ocean equipment including Acoustic Doppler Velocimeter (ADV), Conductivity–Temperature–Depth (CTD) sensors, and Sea Ice Mass Balance Array (SIMBA) was deployed at the landfast ice site, about 1 km far from Zhongshan Station from April to November 2021. The detail of filed observations were described in Section 2. The observations were deeply analysed and oceanic heat flux was estimated by two different methods: residual method and bulk parameterization method, which can be found in the Result section. The relationship between tide and oceanic heat flux, large scale and local phenomena were discussed in Section 4. The conclusions are presented in Section 5.

2 Data and Methods

2.1 Field observations

The field observation was conducted at Zhongshan Station (69°22′ S, 76°22′ E), the second Chinese Antarctic scientific research station, which was established in February 1989 and operated year-round from then on. Zhongshan Station is located in Prydz Bay, East Antarctica (Fig. 1a), and surrounded by 40–100 km width landfast ice in the cold season from February to December (Zhao et al., 2020). In austral summer (i.e., late January), landfast ice usually breaks into small floes due to mechanical forcings like wind, wave, and tide, and then completely disappears (Li et al., 2020), with exception of some small ice floes in the narrow fjords that survived to be the second or multi-year sea ice in the subsequent winter.

From April 16 to November 7, 2021, an integrated ice–ocean interaction observation system was established by the wintering team at the coastal landfast ice site, about 1 km off Zhongshan Station (Fig. 1b). A cable–type CTD (model: ALEC ACTD–DF) was deployed at 2 m beneath the ice surface and 30 m off the shoreline. CTD measured the ocean conductivity, temperature and depth at a frequency of 30 s and the accuracy was ±0.02 mS cm⁻¹ (±0.03 psu) for conductivity (salinity) and ±0.02°C for temperature. An Acoustic Doppler Velocimeter (model: SonTek Argonaut–ADV) was deployed to observe the ocean 3-D velocity, at 5 m below the ice surface and 30 m north of CTD. The frequency for ocean velocity observations was 40 s, and the accuracy was ±0.001 m s⁻¹. A set of Sea Ice Mass Balance Array (model: SRSL SIMBA) was deployed 30 m north of ADV, which contained 240 temperature sensors with 2 cm intervals mounted on the thermistor string, to measure the vertical temperature profile. The SIMBA had a frequency of 6 hours and a resolution of ±0.0625°C (Fig. 1c). The water depth at CTD, ADV and SIMBA sites were 4.5 m, 13 m and 13 m, respectively. Manual observations including snow and ice thickness measurements were conducted every five days by the wintering team, around the integrated ice–ocean interaction observation system.

96   Due to the issues of extreme cold conditions on the battery power supply, the observation system stopped working for part of

97   the period, April 24–May 11 for ADV and July 7–July 15 for CTD. A data quality control was first applied to the original time

98   series, to pick out the anomalous values. To match the different frequencies of ADV and CTD in the inter-comparisons and

99   analysis of oceanic heat flux, the observations were averaged and integrated into a new time series with 2-minute intervals. In

100   processing SIMBA observation data, 3–point smoothing was introduced to minimize the noise influences, which has been used

101   in Zhao et al.(2017).
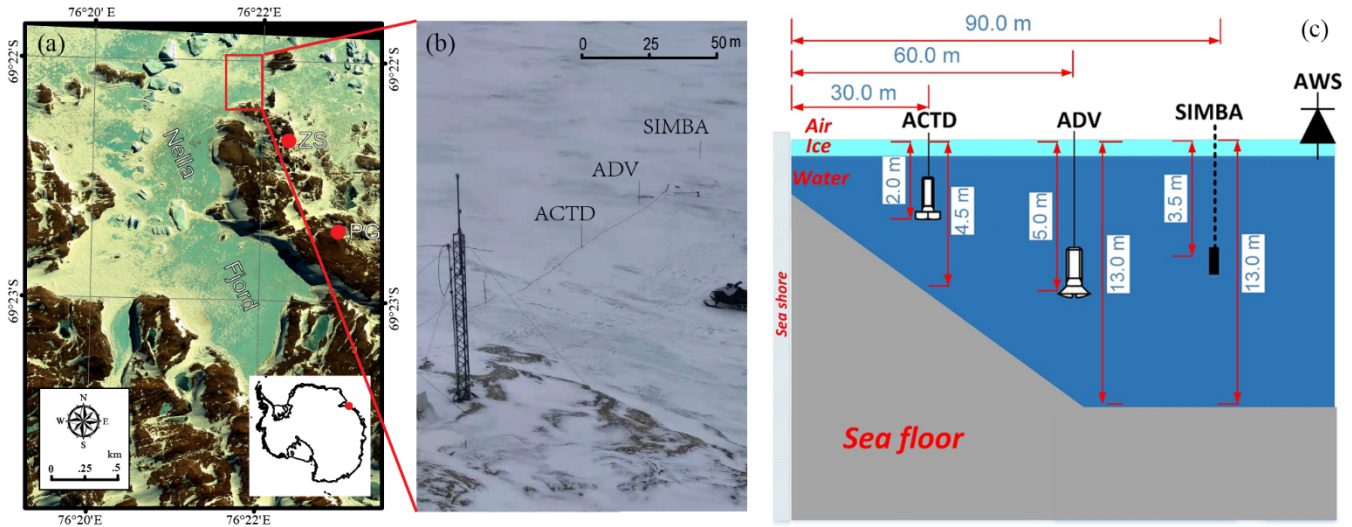
103   **Figure 1. (a) The satellite image of the observation site in Nella Fjord near Zhongshan Station, modified from the WorldView–2**
104   **multi-bands image taken on 20 Oct 2012; (b) The photo of the observation site taken on 12 April 2021 by Jinkai Ma, one of the co-**
105   **authors, when he worked as the wintering team member in Zhongshan Station; (c) Schematic of the integrated ice–ocean interaction**
106   **observation system off Zhongshan Station in 2021.**

107   **2.2 Satellite and reanalysis products.**

108   To further investigate the large-scale influences, satellite and reanalysis products were used here. The AMSR2 sea ice

109   concentration based on the ASI algorithm from the University of Bremen (https://seaice.uni-bremen.de) was adopted to obtain

110   the open water percentage in Prydz Bay, which is daily updated and with a spatial resolution of 6.25 km (Spreen et al., 2008).

111   The Operational Mercator global ocean reanalysis products, produced by Copernicus–Marine Environment Monitoring Service

112   (CMEMS), provided daily and monthly ocean currents and mixed layer depth of the global ocean in a 1/12 degree spatial

113   resolution and 3-hourly frequency (http://marine.copernicus.eu). The large-scale distribution of ocean current and mixed layer

114   depth in Prydz Bay was interpolated into the same spatial resolution as AMSR2 sea ice concentration for comparisons

115   conveniently.

2.3 Methods of oceanic heat flux estimation

2.3.1 Residual method

The residual method was adapted from the classical Stefan Law. By obtaining the measurements of ice vertical temperature profiles and ice bottom growth or ablation, the residual method was used to estimate oceanic heat fluxes widely in previous studies (McPhee and Untersteiner, 1982; Lytle et al., 2000; Perovich and Elder, 2002; Purdie et al., 2006; Lei et al., 2010; Zhao et al., 2019). At the bottom of the sea ice, the heat balance could be expressed by an equilibrium equation as follow:

$$F_w = F_c + F_l + F_s \tag{1}$$

Where F_w is the heat flux from the ocean to the sea ice, F_c is the heat conduction flux through the sea ice, F_l is the latent heat flux caused by the ice freezing or melting, and F_s is the specific heat flux generated by the ice temperature change. In the formula, the signs of melting, heating, and upward heat flow are positive, while the signs of cooling, freezing and downward heat flow are negative.

The three terms of heat fluxes can be further expressed as follows (Semtner, 1976; Lei et al., 2014):

$$F_c = k_i \frac{T_0 - T_f}{H} \tag{2}$$

$$F_l = -\rho_i L_i \frac{dH}{dt} \tag{3}$$

$$F_s = \rho_i c_i \Delta H \frac{dT}{dt} \tag{4}$$

Where k_i is the thermal conductivity of sea ice; T_0 is the ice temperature at the reference layer (detailed in section 3.4); H is the according sea ice thickness; T_f is the freezing point; ρ_i is the ice density; L_i and c_i is the latent and specific heat capacity of sea ice; ΔH is the sea ice thickness of the reference layer; dH/dt is the ice growth rate; dT/dt is the sea ice temperature changes (Untersteiner, 1961; Millero, 1978; McPhee and Untersteiner, 1982; Lei et al., 2010). The density and salinity of landfast ice used here were 910 kg m^{-3} and 4 psu based on the previous observations by Lei et al., 2010. k_i, L_i, and c_i are functions of ice salinity and temperature, and T_f is a function of ocean salinity, which were re-estimated by the CTD observations. The vertical ice temperature gradient, ice growth/melt rate and ice temperature changes were calculated by the SIMBA observations.

2.3.2 Bulk parameterization method

The oceanic heat flux can be determined from direct measurements of high-frequency current velocity, temperature, and salinity in the upper ocean mixed layer beneath ice cover, to evaluate the turbulent heat flux at the ice–ocean interface, called turbulent parameterization method (McPhee, 1992; McPhee et al., 2008). The oceanic heat flux F_w from the ocean mixed layer to the sea ice bottom could be expressed by the following formula (Guo et al., 2015):

$$F_w = \rho_w c_w \langle w'T' \rangle \tag{5}$$

147 Where ρ_w and c_w are the density and specific heat capacity of the ocean mixed layer; $\langle w'T' \rangle$ is the turbulent heat flux. The

148 heat transferred from ocean to ice depends on both the turbulent stress at the ice–ocean interface (characterized by frictional

149 velocity u_0^* as the square root of the kinetic stress at the interface) and the effective heat content of the fluid in the turbulent

150 boundary layer, which is roughly proportional to the deviation of ocean temperature above freezing point (McPhee, 1992;

151 McPhee et al., 1999; Kirillov et al., 2015). Therefore, the turbulent heat flux could be further parameterized as:

$$\langle w'T' \rangle = c_H u_0^* \Delta T \tag{6}$$

153 Where c_H represents the Stanton number of heat exchange efficiency, usually expressed as the difference between the ocean

154 temperature and freezing point; u_0^* is the friction velocity at the interface. For the boundary layer beneath sea ice, the Stanton

155 number c_H usually was assumed constantly to be 0.0057 (McPhee, 2002). Therefore, Eq. (14) could be expressed as:

$$F_w = \rho_w c_w c_H u_0^* \Delta T \tag{7}$$

157 Due to the data's lack of ocean velocity profile and roughness beneath sea ice, the friction velocity u_0^* is usually parameterized

158 by the law of quadratic resistance related to the free-stream current. Here, three different bulk parameterization methods were

159 used to estimate the friction velocity (Table.1). Where, V is absolute flow velocity relative to motionless landfast ice, which

160 was observed by ADV in this study. The velocity perturbation u', v', w' were estimated by removing the mean from the

161 original time series at 15-minute windows.

162

163 **Table 1. Three different Parameterizations of friction velocity u_0^***

Parameterizations	friction velocity	References
Bulk A	$u_0^* = (\langle u'w' \rangle^2 + \langle v'w' \rangle^2)^{1/4}$ (8)	Sirevaag, 2009
Bulk B	$u_0^* = \sqrt{0.0055 * V^2}$ (9)	Kirillov et al., 2015
Bulk C	$u_0^* = \sqrt{0.0104 * V^{1.78}}$ (10)	McPhee, 1979

164 **3 Results**

165 **3.1 Snow and ice evolution**

166 The 4.8 m long SIMBA temperature chains recorded the vertical temperature profiles of air–snow–ice–ocean every 6 hours.

167 Figure 2a showed the observations from 16 April to 7 November 2021, and the serial number of the thermistors starts from the

168 low end in the ocean. The sensor 180 was the initial location of the ice surface on 16 April when SIMBA was deployed in the

169 field, shown as the dotted lines in Figure 2. Typically, the sensors above 180 were located in the air and their temperature

170 showed a significant daily variation. Sea ice temperature showed an obvious gradient, among 0.11–0.24°C cm⁻¹. The ocean

171 temperature was stable, ranging from -1.7°C to -1.9°C, close to the freezing point. The ice bottom was identified by the visual

172 interpretation, according to Zhao et al., (2017), shown as the dashed lines in Figure 2. Ice surface didn't change obviously in

173 the cold season, therefore changes in the ice bottom reflected changes in the ice thickness. The landfast ice was 44.0 cm thick

174   on the first observation day of 16 April, then continued to freeze from May to mid-October, and reached the maximum

175   thickness of 142.0 cm on 22 October. From then on, the ice bottom began to melt at a mean rate of -0.4±0.2 cm d⁻¹ until the

176   observation ended. The annual mean growth rate was 0.5±0.3 cm d⁻¹, and the maximum daily growth rate was 1.6 cm d⁻¹ on

177   May 10, 2021. The monthly mean growth rate was the largest in May (0.8±0.4 cm d⁻¹) and smallest in October (0.1±0.2 cm d⁻

178   ¹), which was similar to the previous observations at Zhongshan Station in 2006 (Lei et al., 2010) and in 2012 (Zhao et al.,

179   2019).

180

181   The vertical gradient of ice temperature profiles showed that snow accumulation on top of ice cover occurred from May to

182   August and dynamic disappearance by strong winds from September (thin black lines in Figure 2b). Finally, snow totally

183   disappeared from October when the air temperature rose up to -2.67°C. Ice surface began to melt under the strong solar

184   radiation, and about 6–8 cm sublimation was observed by SIMBA, shown as the red thin lines. In particular, shortly after

185   SIMBA deployed, the landfast ice thickness experienced a 4 cm decrease during 21–26 April, when the warm air visited the

186   observation site in the cold winter, indicating the influence of short-term weather systems on ice evolution.
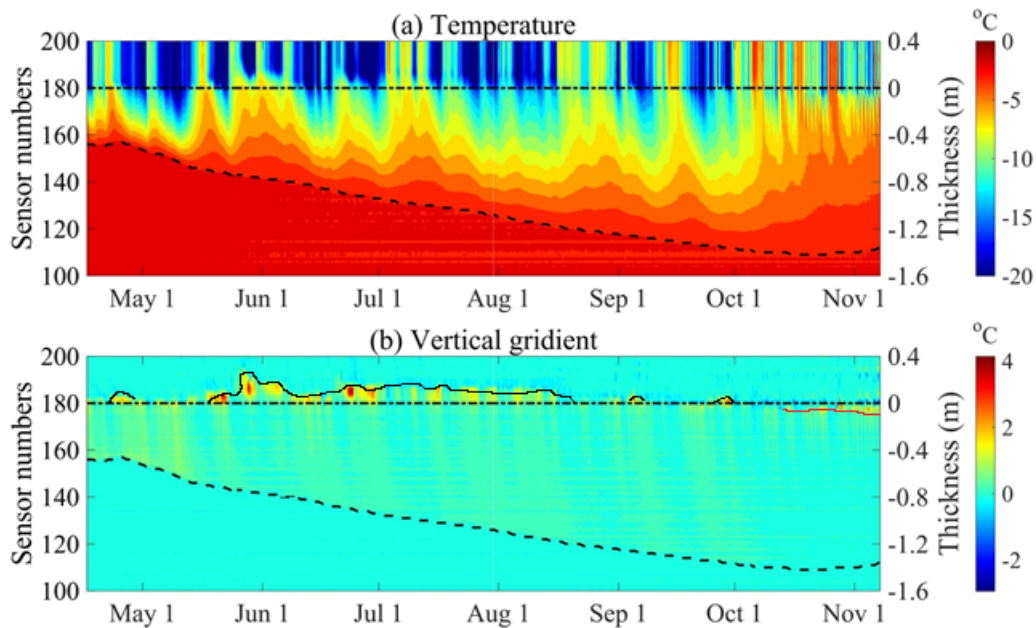
187

188   **Figure 2. The temperature profiles were recorded by SIMBA (a) and the vertical gradient of temperature profiles (b). The black**
189   **dashed line and dotted lines in (a) and (b) represented the ice bottom and initial ice surface, respectively. The black lines and red**
190   **lines in (b) represented the snow surface and new ice surface after sublimation in summer.**

191   **3.2 Ocean temperature, salinity, and density**

192   The times series of ocean temperature were observed by CTD deployed 2 m below the surface of landfast ice. Figure 3a showed

193   the 194 days of high-frequency temperature records at the 2-minute interval, from 16 April to 6 November 2021. The ocean

194 temperature experienced a rapid increase during 16–23 April, from -1.6°C to -1.3°C, then gradually decreased to -1.75°C in
195 the middle of May. In the following months, the ocean temperature remained around -1.79°C and showed a small standard
196 deviation of 0.01°C until the end of observations. Therefore, the ocean beneath the ice was relatively warm and highly variable
197 before the middle of May (-1.64±0.10°C), while dropped and maintained close to the freezing point from then on (-
198 1.79±0.01°C). Based on the spectral analysis, the time series of ocean temperature found an obvious period of 0.5 days, which
199 may relate to the tidal oscillation.

200

201 The temperature at the sea ice bottom (defined as the mean SMIBA sensors temperature at the lowest 10 cm of sea ice) was
202 lower than the ocean temperature, indicating that the heat was transferred from warm water to cold sea ice and inhibited ice
203 bottom growth. During April to May, the temperature at the sea ice bottom showed a large variation (-5–-2.5°C), in response
204 to the variations of air temperature, when the ice was thin and nearly no snow existed. After the thick snow cover formed, the
205 temperature at the sea ice bottom became steady (-2–-3°C) from June to November, along with the stable ocean temperature
206 of around -1.8°C, which attributed to the snow isolation effect on ice and ocean. In particular, when an ice basal melt of 4 cm
207 was recorded by SIMBA during 16 to 26 April, not only a rise in air temperature was observed, but also an increase in ocean
208 temperature occurred, indicating that more heat from both air and ocean was transferred to sea ice, which provided a classic
209 example of air–ice–ocean interactions.

Ocean salinity experienced a quick increase, from 33.3 psu in April to 34.1 psu in May, which was related to the salt rejection processes caused by the large freezing rate of 1.1±0.3 cm d^{-1} at the ice bottom (Figure 3b). More specially, from 19 to 23 April, ocean salinity experienced a short decrease period, different from the long and quick increase trend, which might relate to the slowdown of the ice bottom freezing in those days due to the obvious warming of the air and ocean (Figure 3a). From then on, ocean salinity maintained largely with a small daily and seasonal deviation, around 34.13±0.02 psu, corresponding to a relatively large and stable freezing rate in the ice bottom, around 0.5±0.2 cm d^{-1} until the middle of October. When the warm season came, the sea ice bottom started to melt at a mean rate of -0.4±0.3 cm d^{-1} (from the middle of October to the middle of November), and ocean salinity showed a slight decrease, indicating that the salt rejection became weaker.

As a function of ocean temperature and salinity, ocean density was calculated with the observations measured by CTD, following the equation proposed by Millero and Poisson (1981). Ocean density exhibits a similar trend as ocean salinity, which increased obviously during the early winter, with a mean trend of 0.03 kg m^{-3} day^{-1} (Fig. 3b). In the following observation period, ocean density was stable, with a mean of 1027.47±0.02 kg m^{-3}.

3.3 Ocean current

The 3–D current velocity at 5 m beneath the landfast ice surface was obtained by ADV. Figure 4 showed the velocity in the meridional (U), zonal (V), vertical direction (W), and horizontal speed (the vector sum of U and V). The 2-minute frequency records of U and V showed a large oscillation, mainly varied among ±20 cm s^{-1}, and especially, 97% of U and 96% of V were among ±10 cm s^{-1}. W showed a relatively small oscillation, mainly varied between ±4 cm s^{-1} and 98% of W were among ±2 cm s^{-1}. The typical periods for U, V and W were all 0.5 days.

The rose diagram of the 2-minute records of horizontal current was shown in Figure 5. The domain direction was NWW (-60°) –NEE (60°) and 79% of the velocity was among 5–15 cm s^{-1} (Figure 5a). The horizontal velocity was relatively small in April, smaller than 10 cm s^{-1}, and gradually increased to a maximum in June, when 75% of the velocity was larger than 10 cm s^{-1}. From then on, the horizontal current showed a similar distribution in the directions, while the range of dominated velocity transferred from 10–15 cm s^{-1} to 5–10 cm s^{-1} (Figure 5b–i). The horizontal speed showed an annual mean of 9.5±3.9 cm s^{-1} and a maximum velocity of 29.8 cm s^{-1} for the 2-minute interval records.

244
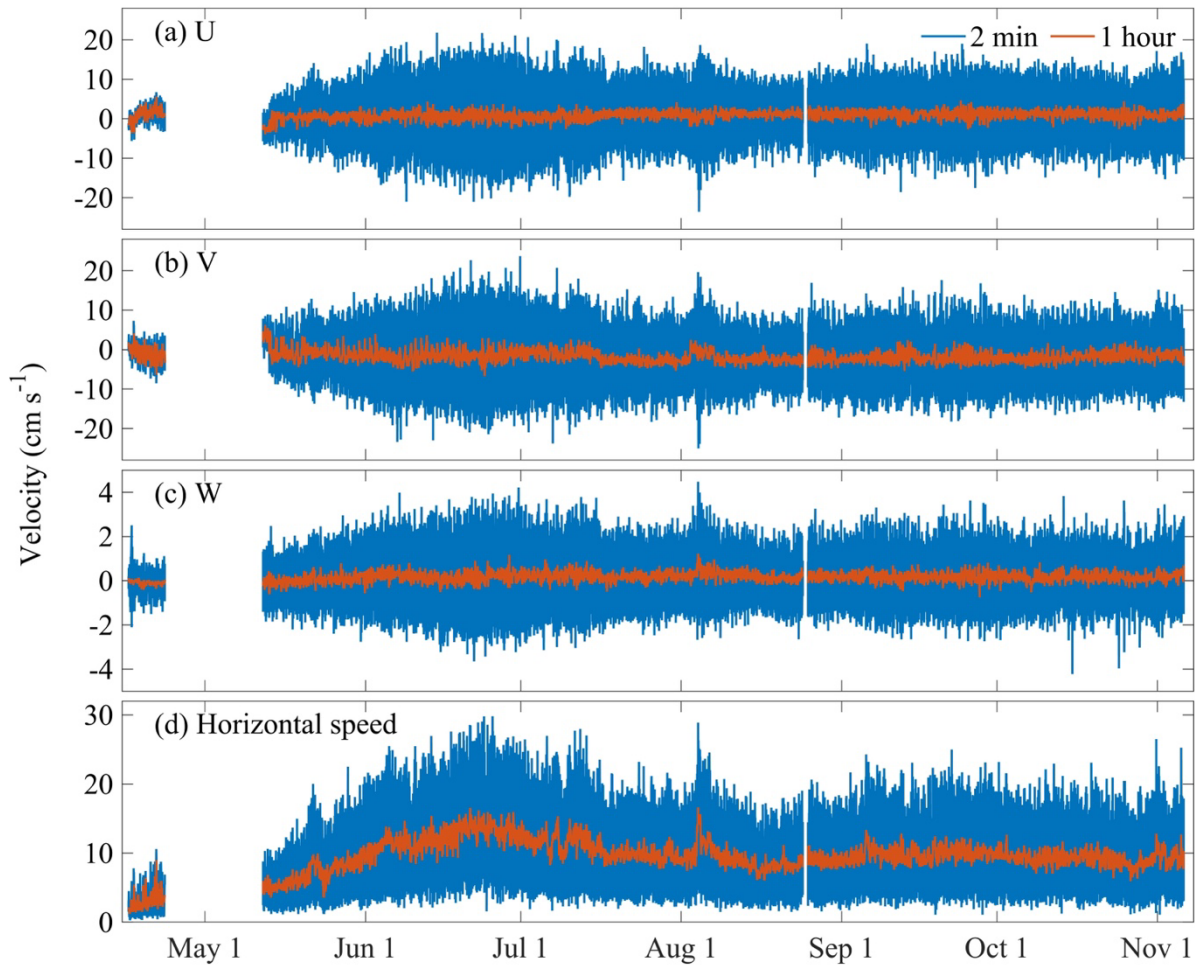
Figure 4. The time series of ocean currents observed by ADV at 5 m beneath landfast ice surface from 16 April to 6 November, 2021.
(a) U, (b) V, (c) W, and (d) horizontal speed.
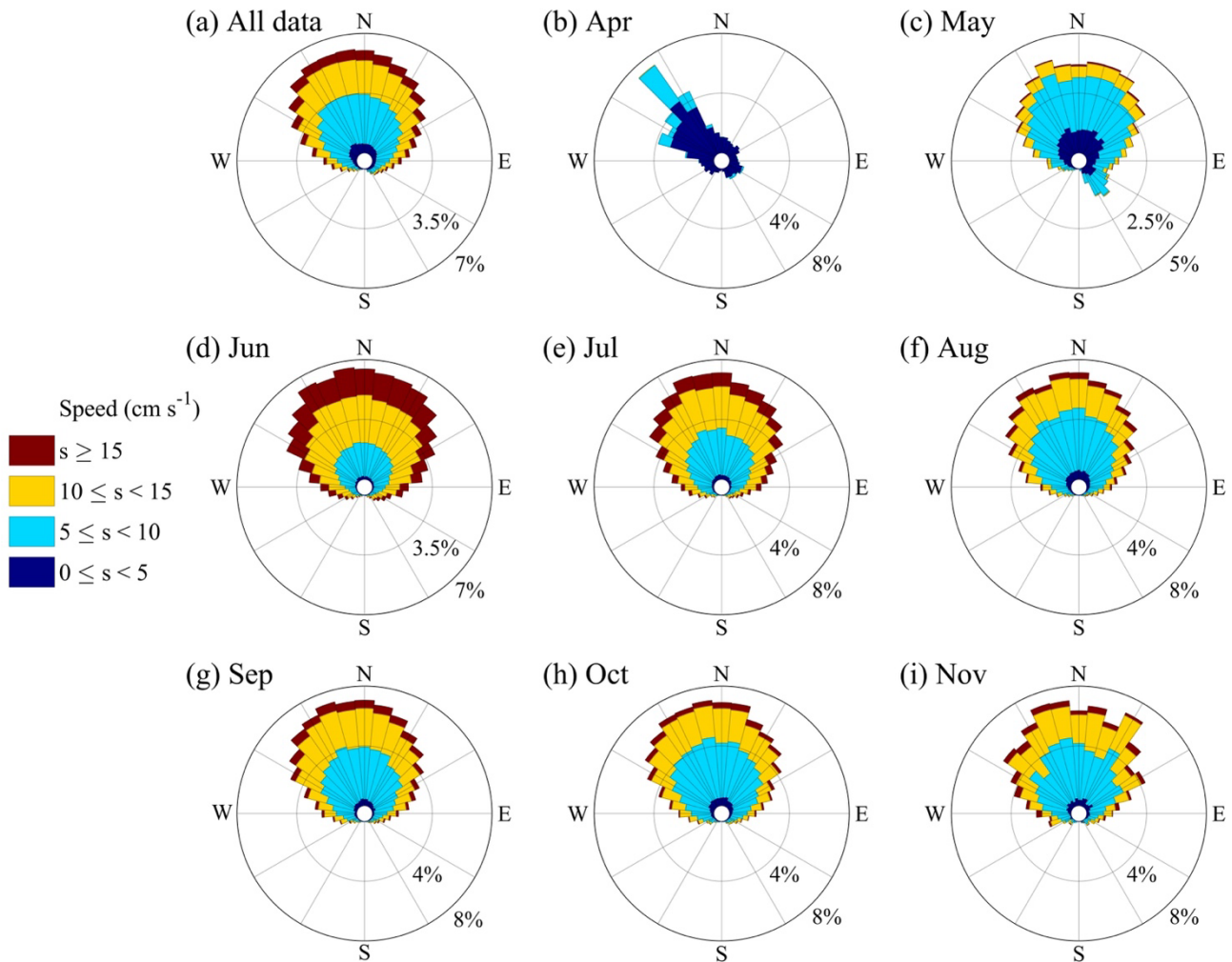
Figure 5. The rose diagram of horizontal current at 2-minute resolution.

3.4 Oceanic heat flux

In the residual method, the vertical gradient of sea ice temperature is a key term for the calculation of conductive heat flux (F_c). In cold and snow–free conditions, surface air temperature and freezing point were usually used to calculate the vertical gradient (Lei et al., 2010; Zhao et al., 2019). However, in the thick snow or warm cases, the vertical temperature profile of the sea ice was not linear anymore. In this study, a reference layer close to the ice bottom was used to calculate the vertical gradient, to avoid nonlinear biases. McPhee and Untersteiner (1982) set the reference layer as about 0.4 m above the ice bottom. Perovich and Elder (2002) chose the reference layer as 0.4–0.8 m above the ice bottom for different ice thickness conditions. Lei et al. (2014) set the reference layer at 0.40–0.70 m above the ice bottom. In this study, we defined the reference layer as 0.2 m above the ice bottom, and the mean vertical gradient was calculated by the 2 cm interval temperatures profile observed by SIMBA.

258

259 In the previous studies, the empirical value of the freezing point usually was used, while a practical one was more realistic in

260 the F_c calculation. Based on the ocean salinity observation by CTD, the freezing points were estimated following the equation

261 in Millero (1978). During the observation period, the freezing points were around -1.83°C in April and gradually decreased to

262 -1.87°C in June, and maintained to November.

263

264 Figure 6 showed the heat fluxes calculated by the residual method. The variation of the latent heat flux (F_l) was strongly

265 correlated with the growth and ablation of sea ice. During the study period, F_l was positive in the cold season, except for a

266 short melt period in April. During 21–24 April, due to the influences of warm air and ocean, SIMBA recorded an obvious

267 melting at the ice bottom and F_l showed a negative value of -20 W m^{-2}. In October, melt season began and F_l transferred to

268 negative. The specific heat flux F_s was smaller throughout the study period, oscillating around 0. The conductive heat flux F_c

269 was relatively large before the middle of May, up to -80 W m^{-2}, then decreased gradually to -20 W m^{-2} in September and finally

270 to -10 W m^{-2} in October and November. The oceanic heat flux showed a larger value of 41.33±9.81 W m^{-2} in April and then

271 decreased to around 10 W m^{-2} from June to October, but quickly increased to 50 W m^{-2} in November before the observation

272 ended. The annual mean of oceanic heat flux for the entire study period was 12.24±10.86 W m^{-2}.
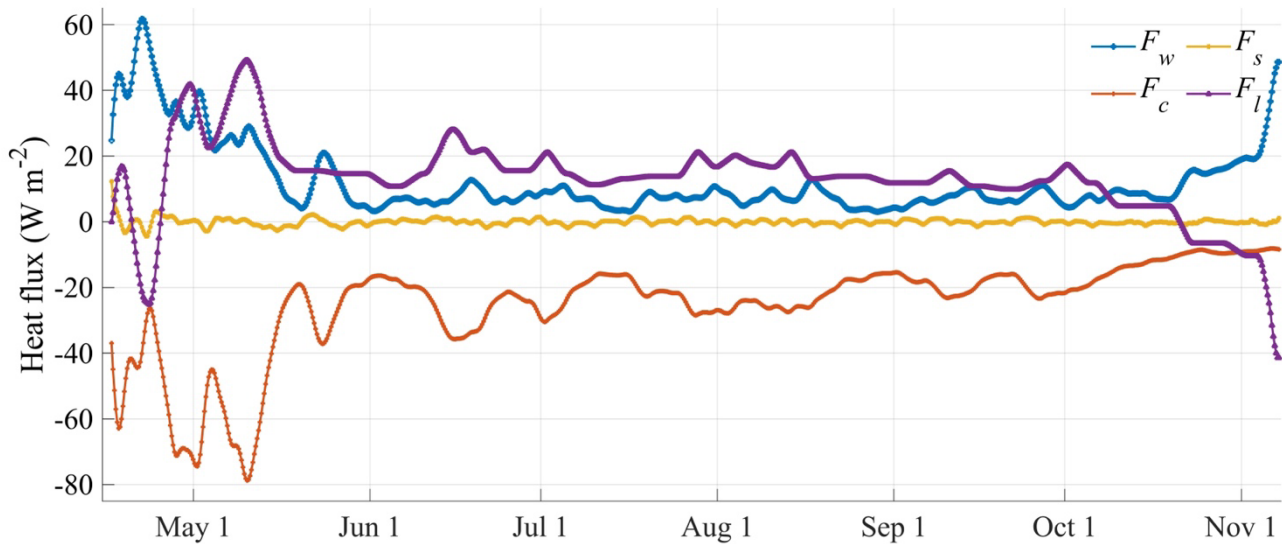
273

274 **Figure 6. Estimated conductive heat flux (F_c), latent heat flux (F_l), specific heat flux (F_s), and oceanic heat flux (F_w) by the residual**
275 **method.**

276 In contrast to the residual method, previous studies had developed the bulk parameterization methods to calculate the oceanic

277 heat flux when the observations of ocean parameters were available (McPhee, 1979, 1992; Sirevaag, 2009; Kirillov et al.,

278 2015). In this study, ocean velocity, temperature, and salinity in the ice–ocean boundary layer were recorded at a high

279 frequency by ADV and CTD, which provided a chance to evaluate the oceanic heat flux by the bulk parameterized methods.

280

281   During the observation period, ocean temperature was always warmer than the freezing point, indicating that the heat flux was

282   transferred from the ocean to ice. The temperature difference (ΔT) between the ocean and the freezing point was 0.26±0.08°C

283   in April and decreased gradually to 0.08°C from June to November. Three different bulk parameterized methods were used

284   here (Bulk A: Sirevaag, 2009; Bulk B: Kirillov et al., 2015; Bulk C: McPhee, 1979), and their main differences came from the

285   expressions of the fraction velocity and empirical parameters, as listed in Table.1.

286

287   The hourly oceanic heat flux calculated by three bulk parameterized methods showed similar variations, high to 60–80 W m^{-2}

288   in April, and then gradually decreased to 10–30 W m^{-2}, as the results from the residual method. The annual mean oceanic heat

289   flux were 19.73±5.32 W m^{-2}, 13.64±3.12 W m^{-2}, and 24.35±5.35 W m^{-2} for Bulk A, Bulk B, and Bulk C, respectively, and

290   12.24±10.86 W m^{-2} for residual method (Fig. 7a). The bulk methods were 8.97±8.98 W m^{-2} larger than the residual method on

291   average during the study period.

292

293   According to the monthly oceanic heat flux shown in Fig. 7b, oceanic heat flux were 18.39 W m^{-2}, 15.72 W m^{-2}, 31.38 W m^{-}

294   ^{2}, and 41.33 W m^{-2} in April for Bulk A, Bulk B, Bulk C, and residual methods, respectively. In the meantime, oceanic heat

295   flux had a large standard deviation in April, 10–20 W m^{-2} for the bulk methods and 10 W m^{-2} for the residual method, indicating

296   a large variation in the hourly time series. From May to October, the standard deviations were generally smaller than 5 W m^{-}

297   ^{2}. Among the three bulk parameterization methods, Bulk C was relatively larger than Bulk A and B.

298

299   Previous studies estimated the oceanic heat flux under landfast ice in Prydz Bay with different methods. Allison (1981)

300   estimated oceanic heat flux near Mawson Station from monthly mean temperature and ice growth. At the early stage of sea ice

301   growth, the thermohaline convection caused by the brine rejection makes the flux very high, which could be as high as 50 W

302   m^{-2}. Heil et al. (1996) used a multilayer thermodynamic model to simulate sea ice growth at Mawson Station. The multi-year

303   averaged oceanic heat flux estimated by daily values was 7.9 W m^{-2}, and the annual mean was between 5 and 12 W m^{-2} from

304   1958 to 1986. Lei et al. (2010) estimated the oceanic heat flux near Zhongshan Station in early April to be 15–20 W m^{-2}. Yang

305   et al. (2016) estimated the oceanic heat flux by a thermodynamic model and the result was 25 W m^{-2} in March–April. According

306   to the weekly observation near Zhongshan Station, Zhao et al. (2019) interpolated and calculated the daily oceanic heat flux

307   from March to May to be 30.0 W m^{-2}. In this study, the averaged oceanic heat flux calculated by the residual method and the

308   bulk methods were consistent with the previous studies but based on a higher temporal resolution (6 hours for the residual

309   method and 2 minutes for the bulk methods), which provided more detail to the readers and communities.

310
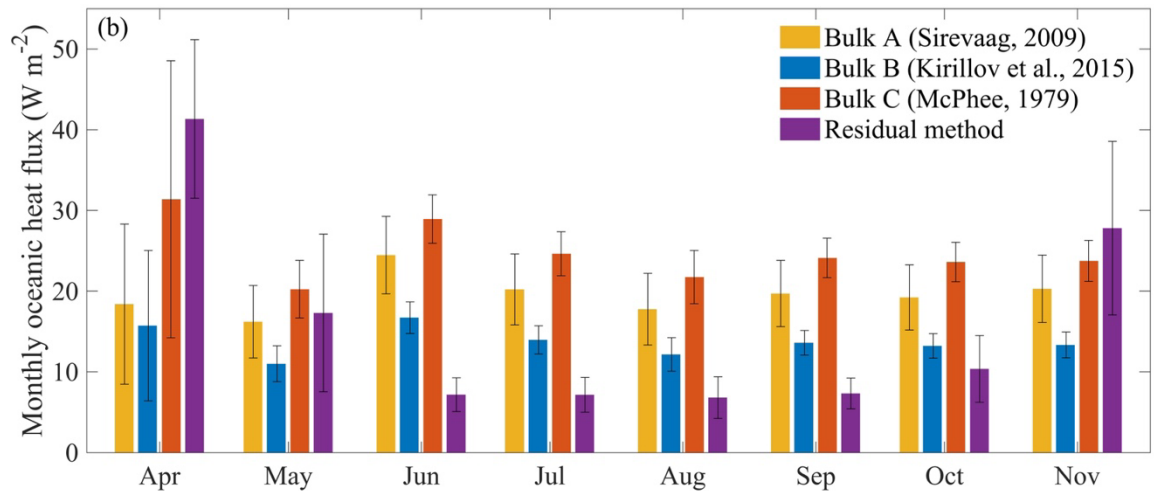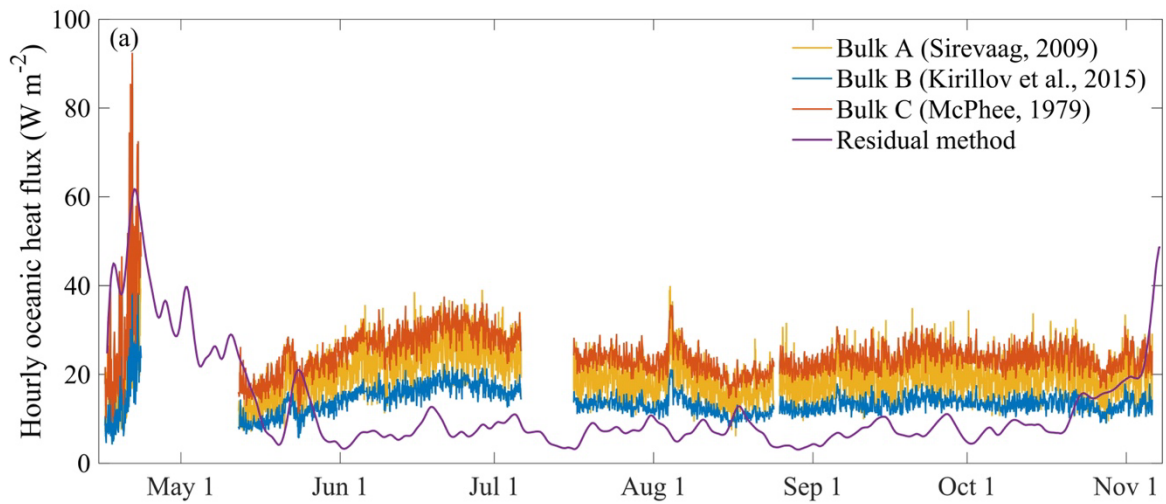
Figure 7. Hourly (a) and monthly (b) oceanic heat flux, calculated by three bulk parameterization methods and residual method.

Table 2. Inter-comparisons of mean oceanic heat flux (W m⁻²) calculated by different methods

Methods	Apr	May	Jun	Jul	Aug	Sep	Oct	Nov	Totally
Residual method	41.33±9.81	17.30±9.75	7.17±2.08	7.16±2.15	6.81±2.57	7.32±1.90	10.36±4.14	27.80±10.75	12.24±10.86
Bulk A	18.39±9.92	16.21±4.49	24.46±4.80	20.21±4.38	17.76±4.44	19.70±4.10	19.22±4.04	20.28±4.17	19.73±5.32
Bulk B	15.72±9.31	10.99±2.22	16.72±1.96	13.96±1.74	12.16±2.08	13.60±1.53	13.21±1.51	13.32±1.59	13.64±3.12
Bulk C	31.38±17.16	20.23±3.56	28.93±2.99	24.63±2.72	21.74±3.30	24.11±2.45	23.61±2.44	23.75±2.54	24.35±5.35

4. Discussions

4.1 The potential influences of local tide oscillations

The local tide may influence the evolution of sea ice (Lei et al., 2009). The tide oscillations were reconstructed by the harmonic analysis method (Pan et al., 2018), using the harmonic constants from E et al., (2013). The spectral analysis showed that the tide oscillations showed two PSD peaks, the largest one referred to the period of 1 day and the second largest one referred to 0.5 days, which indicated that the tide type was irregular diurnal tide near Zhongshan Station (Figure 8). To further investigate the relationship between tide oscillations and oceanic variables, the same spectral analysis was employed for all the observed ocean variables. Ocean temperature showed the largest peak at the period of 1 day and a relatively low peak at the period of 0.5 days, while ocean salinity, U, V, W, and the results from three bulk parameterization methods showed the largest peak at the period of 0.5 days and a relatively low peak of 1 day (Figure 9). Those results from spectral analysis indicated that ocean temperature, salinity, U, V, W, as well as oceanic heat flux were largely affected by the tide oscillations.
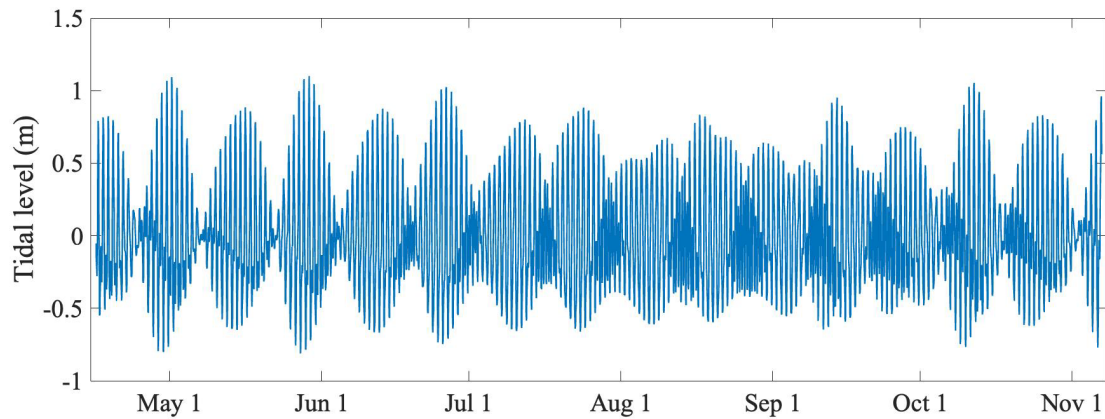
Figure 8. The constructed tide oscillations by the harmonic analysis method (Pan et al., 2018), using the harmonic constants from E et al., (2013).
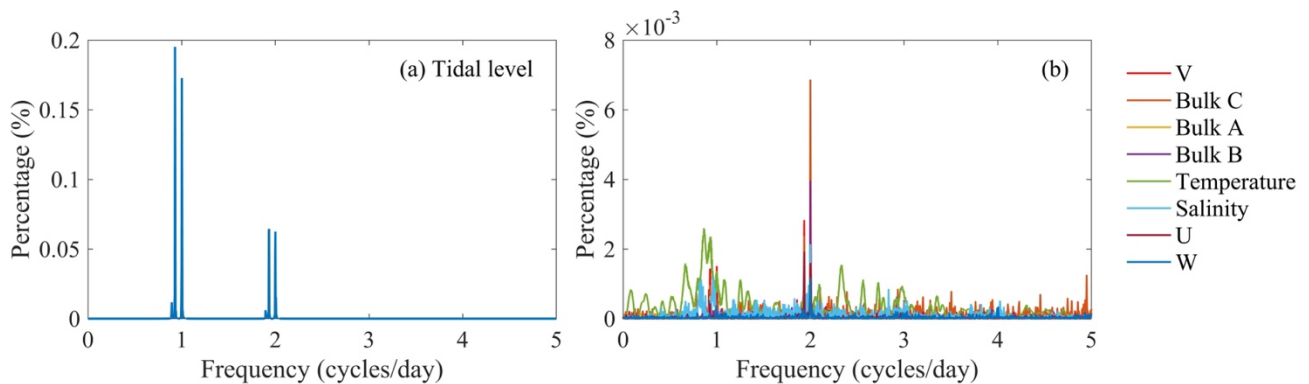
Figure 9. The results of spectral analysis for the tide oscillation (a), and the observed ocean variables, as well as the calculated F_w (b).

In April, observed ocean temperature and salinity showed a special pattern that the water was relatively warm and fresh in the equilibrium tide state, while cold and salty in the low and high tide state (Figure 10a, b), which may relate to the efficient horizontal heat transport when the surrounding area was not covered by ice totally. However, in other months, the larger observed vertical velocity shown in Figure 4 enhanced the vertical mixing, therefore no significant variation was found in the ocean temperature and salinity, as well as oceanic heat flux during the same period.

What is more, when the tide level changed from low to high, hourly U changed from a slightly positive distribution (0.67 ± 1.21 cm s^{-1}) to a deeply positive distribution (1.15 ± 1.14 cm s^{-1}), indicating a dominated eastward flow for high tide level condition (Figure 10c). V changed from a slightly negative distribution (-1.25 ± 1.63 cm s^{-1}) to an intensively negative distribution (-2.14 ± 1.34 cm s^{-1}), which suggested the southward flow became stronger when the tide level went high (Figure 10d). W varied unapparent, and the mean were almost the same, 0.17 ± 0.25 cm s^{-1} and 0.17 ± 0.23 cm s^{-1}, respectively for the low and high tide levels (Figure 10e).

346
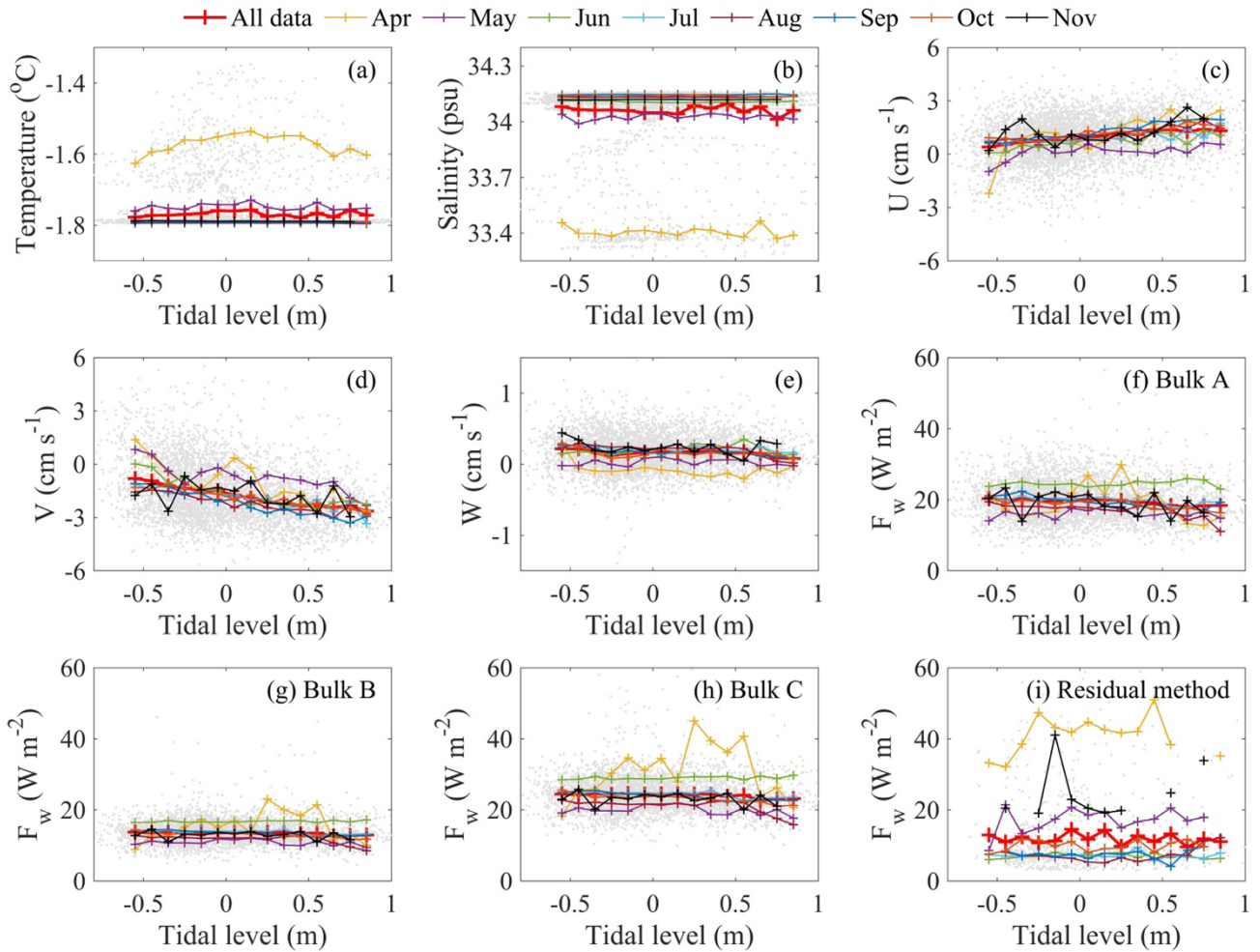
Figure 10. The scatter plot between tidal level and oceanic variables. The different lines represented the monthly mean of the according variables binned by 0.1 tidal level.

4.2 The relationships between large-scale and local phenomena

Prydz Bay was covered by sea ice in the cold season. Ice floes appeared widely in March, while landfast ice started to form one month later in April near Zhongshan Station. From May to October, ice floes covered the entire Prydz Bay, except for several polynyas, and in the meantime, landfast ice extended gradually to around 100 km along the zonal direction. In November, ice floe concentration decreased, while landfast ice cover reached its maximum extent (Figure 11). The open water area was nearly 80% of the entire ocean grid in March, allowing more solar heat flux absorbed by the ocean, which was the energy basis for the warm ocean in April (Figure 12). The large-scale circulation in Prydz Bay indicated a westward current along the Antarctic coastline, stronger in the ice–free and low–concentration months, and weaker in the high–concentration months. In April, the large-scale current carried the warm water from low latitude to high latitude, contributing to the observed

rise of ocean temperature near Zhongshan Station. From then on, polar night came, the air temperature dropped, the ice cover concentrated, less solar radiation penetrated into the ocean, the large-scale current weakened, and the horizontal heat transport decreased (Figure 13).

The ocean mixed layer shown in Figure 13 demonstrated an obvious thick from May to October, which may relate to the strengthened vertical mixing caused by the salt rejection when sea ice continued to grow. The large ocean salinity observed by CTD near Zhongshan Station (green lines in Figure 12) confirmed this assumption. Considering the decreased horizontal heat transport, the evolution of ocean temperature was mainly affected by local factors. In this study, the observation was conducted close to the shore with a water depth of around 10 m, making the full mixing of the shallow water possible. Therefore, ocean temperature remained at a stable level from June to November (red lines in Figure 12).

The water depth near the shoreline may affect the capacity of vertical mixing. The observations of ocean temperature from SIMBA sensors at 2 m beneath the ice surface and CTD were obviously different (annual mean difference was -0.17±0.03°C), which is largely beyond the errors of the instruments. The water depth for SIMBA and CTD was 4.5 m and 13 m, respectively, which was believed to cause the different vertical mixing strengths and then the different ocean temperatures.
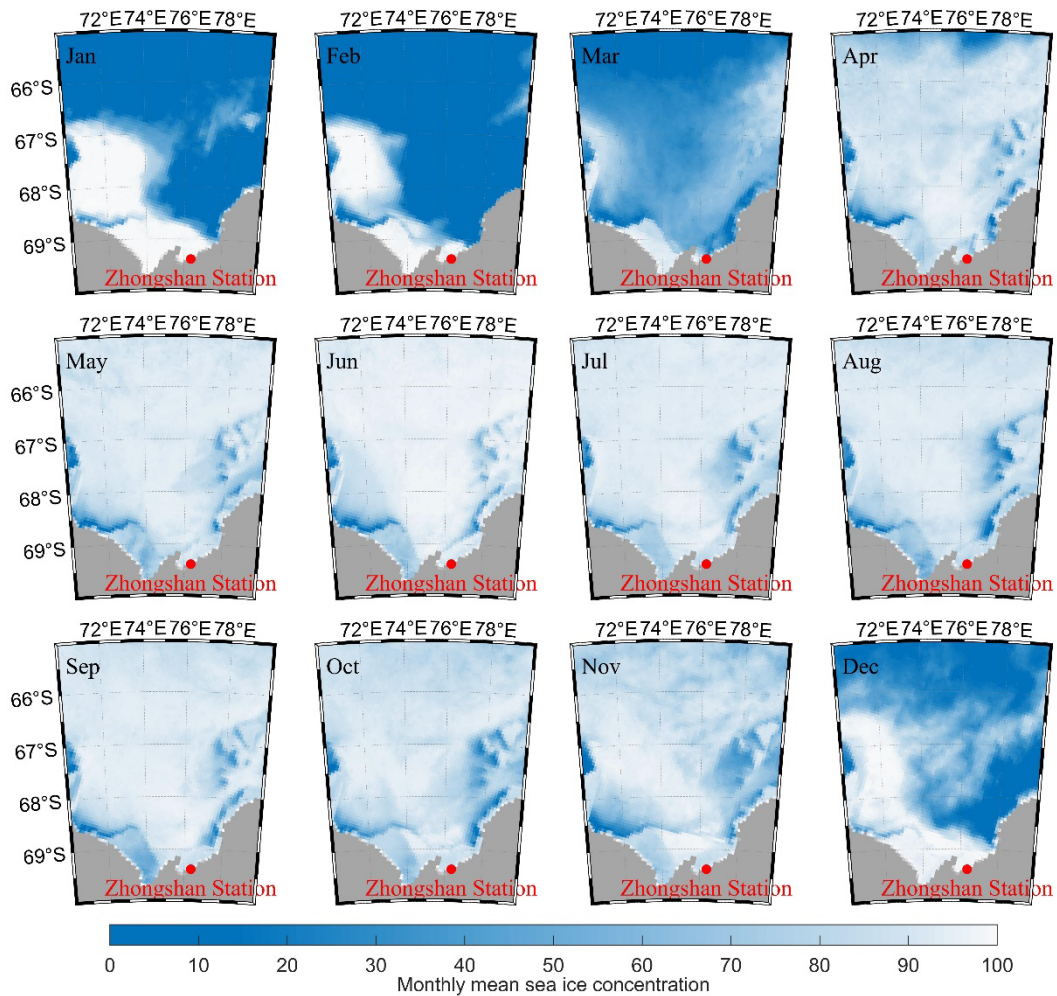
Figure 11. The evolution of monthly sea ice concentration in Prydz Bay in 2021, retrieved from the AMSR2 product provided by the Bremen University.
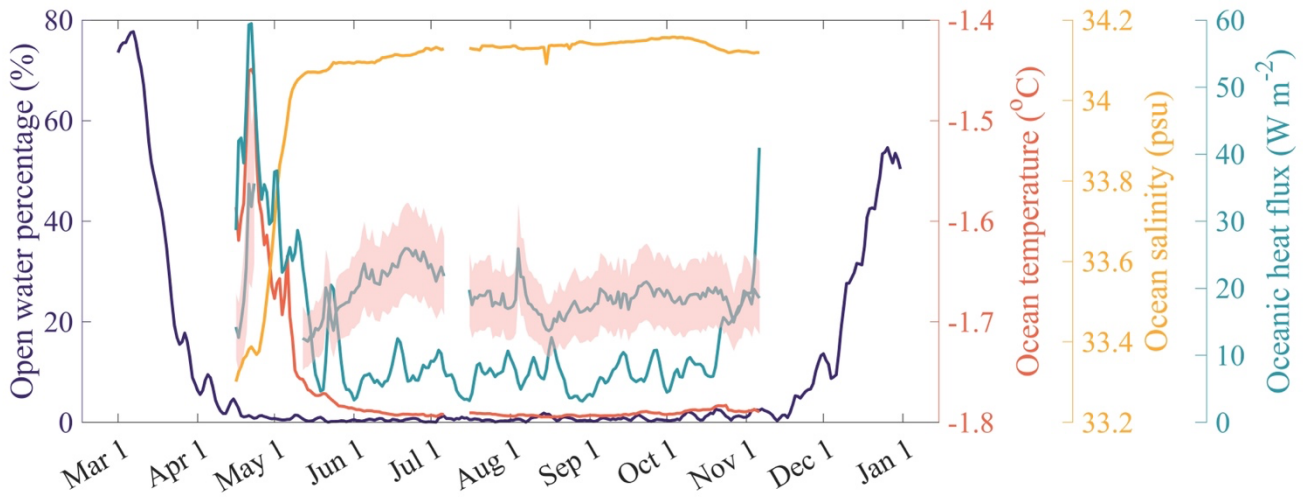
Figure 12. The time series of daily open water percentage and ocean variables in 2021. Open water was defined as sea ice concentration smaller than 15%.
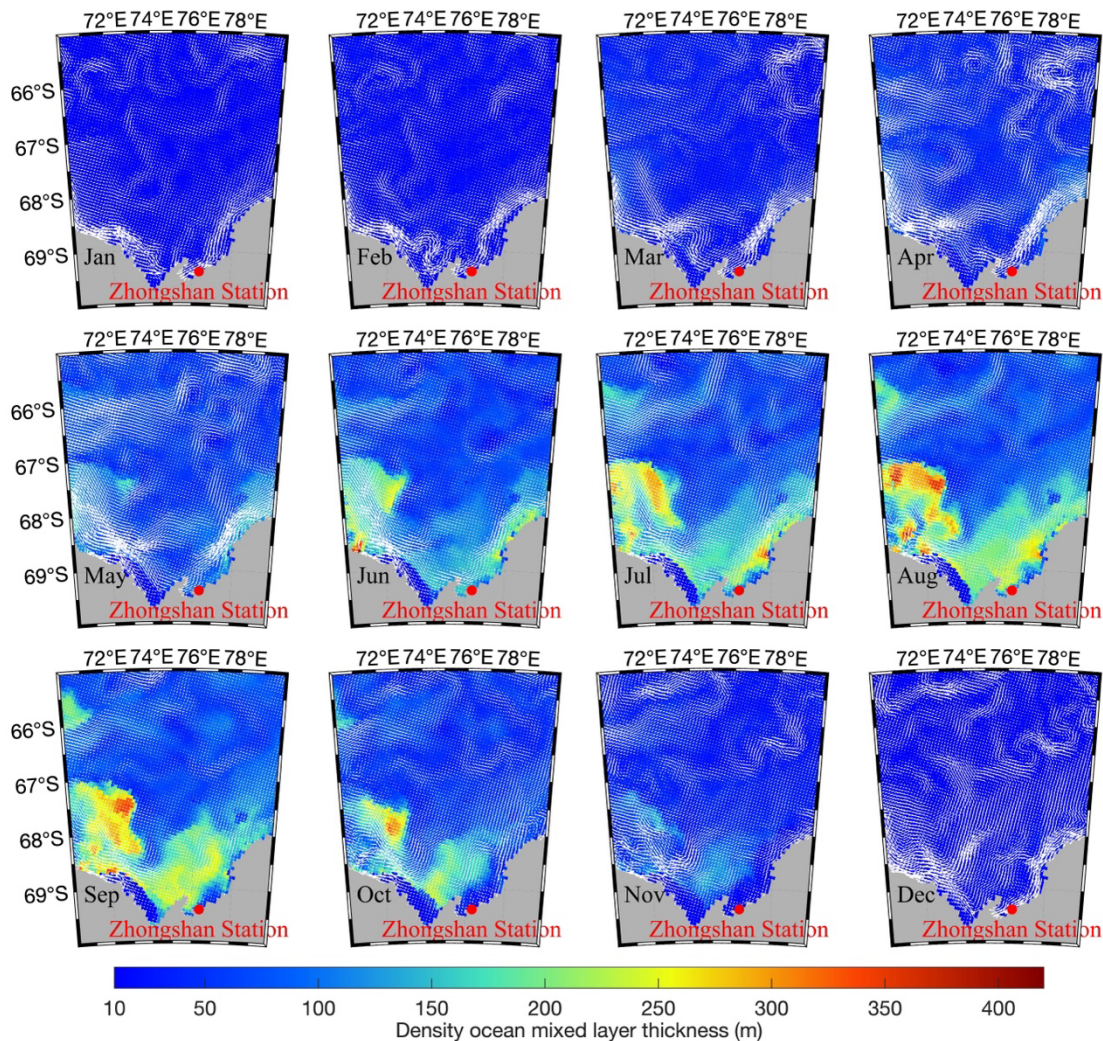
Figure 13. The large-scale ocean circulation for different months in 2021 in Prydz Bay, was derived from the Mercator Ocean reanalysis.

5 Conclusions

The heat and monument balance among air–ice–ocean was one of the most important processes in the Polar Regions. The air–ice interaction has been well investigated, due to the fact that on–ice observation is relatively easy to conduct. However, the ice–ocean interaction was rarely studied because of the difficulty and limit of underwater observations. The oceanic boundary layer beneath sea ice plays an important role in the growth and melting of sea ice. In this study, an integrated ice–ocean observation system including ADV, CTD, and SIMBA was deployed on the landfast ice, 1 km far from Zhongshan Station in

388   Prydz Bay, East Antarctica. The minute-resolution and 8 month long ocean temperature, salinity, and velocity were observed

389   and investigated for the first time in this region.

390

391   The SIMBA temperature chain recorded vertical temperature profiles of air–snow–ice–ocean, which was used to estimate

392   snow and ice thickness and oceanic heat flux by the residual method. The results show that landfast ice froze 98 cm at the

393   bottom from April to October, with a mean rate of 0.5 ± 0.3 cm d^{-1}, and melted 4 cm in November, with a rate of -0.4±0.2 cm

394   d^{-1} until the observation ended. About 6–8 cm surface sublimation was observed in summer. The maximum snow thickness

395   was around 30 cm in May and maintained at 10–20 cm until August. CTD recorded minute-resolution ocean temperature and

396   salinity at 5 m depth beneath the ice surface. Ocean temperature showed a jump increase from -1.6°C to -1.3°C in April, then

397   gradually decrease to -1.75°C in May. Ocean temperature from June to November remained stable, with a mean of -

398   1.79±0.01°C. In April, landfast ice was 44–50 cm thick and snow free on the ice surface, therefore the variation of air

399   temperature showed a large influence on ice and ocean temperature. The significant increase in air and ocean temperature led

400   to the temperature rise in the ice bottom and then contributed to the sudden melt of 4 cm in the ice bottom observed by SIMBA.

401   The thick snow cover from May to August provided an isolation layer for ice and ocean, then contributed to the stable ocean

402   temperature during the according to period.

403

404   The ocean salinity experienced an increase from 33.33 psu in April to 34.08 psu in May, with a trend of 0.04 psu d^{-1}. From

405   June to November, ocean salinity was stable around 34.13±0.02 psu. The ocean density calculated by observed ocean salinity

406   increased from 1026.83 kg m^{-3} to 1027.42 kg m^{-3} from April to May and maintained at 1027.47±0.01 kg m^{-3} from then on. The

407   ocean velocity was recorded by ADV from April to November. The analysis of the 2-minute resolution time series showed

408   that 79% of the ocean velocity was among 5–15 cm s^{-1} and the annual mean was 9.5±3.9 cm s^{-1}. The maximum velocity was

409   29.8 cm s^{-1}, observed on June 25, 2021. The dominant current direction was NWW (-60°) –NEE (60°). The spectral analysis

410   suggested a typical period of 0.5 days for U, V, and W, which may relate to the tide oscillation near Zhongshan Station. The

411   meridional velocity V was dominated by the southward flow and became stronger when the tide level went higher.

412

413   The oceanic heat flux was estimated by the residual method and three different bulk parameterization methods. The results

414   showed a similar peak among 60–80 W m^{-2} in April-May and decreased to a stable level of 10–30 W m^{-2} from then on. The

415   annual mean was 12.24±10.86 W m^{-2} for the residual method and 19.73±5.32 W m^{-2}, 13.64±3.12 W m^{-2}, and 24.35±5.35 W

416   m^{-2}, respectively for three bulk parameterization methods. The large differences were mainly caused by the different formulas

417   of friction velocity, indicating the uncertainties of the empirical equation. The estimated results in this study were consistent

418   with previous studies, which are usually based on low-frequency observations of ice thickness. The oceanic heat fluxes showed

419   a similar period of 0.5 days, believed to relate to the tide oscillation, too.

420

The observations of ocean temperature, salinity, U, V, and W, as well as the estimation of ocean density and oceanic heat flux, showed similar periods as the local tide oscillation, suggesting tide was one of the main drivers of oceanic variations near Zhongshan station. Large-scale sea ice distribution and current transformation affected the solar radiation absorption by the upper ocean and the horizontal heat transport, which was another main driver of oceanic variations near Zhongshan station. Both local and large-scale influences play important roles in the oceanic heat flux, further the ice–ocean interactions.

In this study, the high-frequency oceanic measurements provide a chance to investigate the detail of ice–ocean interactions beneath landfast ice on the diurnal and seasonal scale. The bulk parameterization was first used to estimate the oceanic heat flux near Zhongshan Station, providing more interesting information compared to the residual method. More ice and ocean equipment, like ice thickness radar, ocean temperature chains, ice salinity gauge, and so on will be considered in the future, to fill the data gap we still missed in this study.

Data availability

Observation data are available upon request to the corresponding author.

Author contributions

JC conceptualized this study and designed the numerical methods. HH carried out the experiments and wrote the manuscript. JC, PH and FH helped analyse the results and revised the manuscript. JM provided and helped process the sea ice observation data. XC assisted during the writing progress and critically discussed the contents.

Competing interests

One of the co-authors is a member of the editorial board of *The Cryosphere*, and the authors also have no other competing interests to declare.

Acknowledgement

This study is financially supported by the National Natural Science Foundation of China (41876212). PH was supported by the Australian Government through Australian Antarctic Science projects 4506 and the International Space Science Institute grant no. 406.

References

Allison, I.: Antarctic ice growth and oceanic heat flux, Sea level, ice and climatic change, 131, 161–170, 1981.

Cheng, B., Vihma, T., Pirazzini, R., and Granskog, M. A.: Modelling of superimposed ice formation during the spring snowmelt period in the Baltic Sea, Ann. Glaciol., 44, 139–146, https://doi.org/10.3189/172756406781811277, 2006.

Clem, K. R., Fogt, R. L., Turner, J., Lintner, B. R., Marshall, G. J., Miller, J. R., and Renwick, J. A.: Record warming at the South Pole during the past three decades, Nat. Clim. Chang., 10, 762–770, https://doi.org/10.1038/s41558-020-0815-z, 2020.

Comiso, J. C., Parkinson, C. L., Gersten, R., and Stock, L.: Accelerated decline in the Arctic sea ice cover, Geophys. Res. Lett., 35, L01703, https://doi.org/10.1029/2007GL031972, 2008.

E, D., Huang, J., and Zhang, S.: Analysis of Tidal Features of Zhongshan Station, East Antarctic, Geomatics and information science of WUHAN UNIVERSITY, 379-382+464, https://doi.org/10.13203/j.whugis2013.04.025, 2013 (in Chinese).

Fedotov, V. I., Cherepanov, N. V., and Tyshko, K. P.: Some Features of the Growth, Structure and Metamorphism of East Antarctic Landfast Sea Ice, in: Antarctic Research Series, edited by: Jeffries, M. O., American Geophysical Union, Washington, D. C., 343–354, https://doi.org/10.1029/AR074p0343, 2013.

Fraser, A. D., Massom, R. A., Handcock, M. S., Reid, P., Ohshima, K. I., Raphael, M. N., Cartwright, J., Klekociuk, A. R., Wang, Z., and Porter-Smith, R.: Eighteen-year record of circum-Antarctic landfast-sea-ice distribution allows detailed baseline characterisation and reveals trends and variability, The Cryosphere, 15, 5061–5077, https://doi.org/10.5194/tc-15-5061-2021, 2021.

Giles, K. A., Laxon, S. W., and Ridout, A. L.: Circumpolar thinning of Arctic sea ice following the 2007 record ice extent minimum, Geophys. Res. Lett., 35, L22502, https://doi.org/10.1029/2008GL035710, 2008.

Guo, G., Shi, J., and Jiao, Y.: Temporal variability of vertical heat flux in the Makarov Basin during the ice camp observation in summer 2010, Acta Oceanol. Sin., 34, 118–125, https://doi.org/10.1007/s13131-015-0755-z, 2015.

Heil, P.: Atmospheric conditions and fast ice at Davis, East Antarctica: A case study, J. Geophys. Res., 111, C05009, https://doi.org/10.1029/2005JC002904, 2006.

Heil, P., Allison, I., and Lytle, V. I.: Seasonal and interannual variations of the oceanic heat flux under a landfast Antarctic sea ice cover, J. Geophys. Res., 101, 25741–25752, https://doi.org/10.1029/96JC01921, 1996.

475 Kirillov, S., Dmitrenko, I., Babb, D., Rysgaard, S., and Barber, D.: The effect of ocean heat flux on seasonal ice growth in
476 Young Sound (Northeast Greenland): THE OCEAN HEAT FLUX IN YOUNG SOUND FJORD, J. Geophys. Res. Oceans,
477 120, 4803–4824, https://doi.org/10.1002/2015JC010720, 2015.

478 Launiainen, J. and Cheng, B.: Modelling of ice thermodynamics in natural water bodies, Cold Regions Science and
479 Technology, 27, 153–178, https://doi.org/10.1016/S0165-232X(98)00009-3, 1998.

480 Lei, R., Li, Z., Cheng, Y., Wang, X., and Chen, Y.: A New Apparatus for Monitoring Sea Ice Thickness Based on the
481 Magnetostrictive-Delay-Line Principle, Journal of Atmospheric and Oceanic Technology, 26, 818–827,
482 https://doi.org/10.1175/2008JTECHO613.1, 2009.

483 Lei, R., Li, Z., Cheng, B., Zhang, Z., and Heil, P.: Annual cycle of landfast sea ice in Prydz Bay, east Antarctica, J. Geophys.
484 Res., 115, C02006, https://doi.org/10.1029/2008JC005223, 2010.

485 Lei, R., Li, N., Heil, P., Cheng, B., Zhang, Z., and Sun, B.: Multiyear sea ice thermal regimes and oceanic heat flux derived
486 from an ice mass balance buoy in the Arctic Ocean: ARCTIC SEA-ICE THERMAL REGIMES, J. Geophys. Res. Oceans,
487 119, 537–547, https://doi.org/10.1002/2012JC008731, 2014.

488 Li, X., Shokr, M., Hui, F., Chi, Z., Heil, P., Chen, Z., Yu, Y., Zhai, M., and Cheng, X.: The spatio-temporal patterns of
489 landfast ice in Antarctica during 2006–2011 and 2016–2017 using high-resolution SAR imagery, Remote Sensing of
490 Environment, 242, 111736, https://doi.org/10.1016/j.rse.2020.111736, 2020.

491 Liu, J. and Curry, J. A.: Accelerated warming of the Southern Ocean and its impacts on the hydrological cycle and sea ice,
492 Proceedings of the National Academy of Sciences, 107, 14987–14992, https://doi.org/10.1073/pnas.1003336107, 2010.

493 Lytle, V. I., Massom, R., Bindoff, N., Worby, A., and Allison, I.: Wintertime heat flux to the underside of East Antarctic
494 pack ice, J. Geophys. Res., 105, 28759–28769, https://doi.org/10.1029/2000JC900099, 2000.

495 Manabe, S. and Stouffer, R. J.: Sensitivity of a global climate model to an increase of CO_2 concentration in the atmosphere,
496 J. Geophys. Res., 85, 5529, https://doi.org/10.1029/JC085iC10p05529, 1980.

497 Massom, R. A. and Stammerjohn, S. E.: Antarctic sea ice change and variability – Physical and ecological implications,
498 Polar Science, 4, 149–186, https://doi.org/10.1016/j.polar.2010.05.001, 2010.

499 Massom, R. A., Hill, K. L., Lytle, V. I., Worby, A. P., Paget, M. J., and Allison, I.: Effects of regional fast-ice and iceberg
500 distributions on the behaviour of the Mertz Glacier polynya, East Antarctica, Ann. Glaciol., 33, 391–398,
501 https://doi.org/10.3189/172756401781818518, 2001.

502 Maykut, G. A. and Untersteiner, N.: Some results from a time-dependent thermodynamic model of sea ice, J. Geophys. Res.,
503 76, 1550–1575, https://doi.org/10.1029/JC076i006p01550, 1971.

504 McPhee, M. G.: The Effect of the Oceanic Boundary Layer on the Mean Drift of Pack Ice: Application of a Simple Model, J.
505 Phys. Oceanogr., 9, 388–400, https://doi.org/10.1175/1520-0485(1979)009<0388:TEOTOB>2.0.CO;2, 1979.

506 McPhee, M. G.: Turbulent heat flux in the upper ocean under sea ice, J. Geophys. Res., 97, 5365,
507 https://doi.org/10.1029/92JC00239, 1992.

508 McPhee, M. G.: Turbulent stress at the ice/ocean interface and bottom surface hydraulic roughness during the SHEBA drift,

509 J. Geophys. Res., 107, 8037, https://doi.org/10.1029/2000JC000633, 2002.

510 McPhee, M. G. and Untersteiner, N.: Using sea ice to measure vertical heat flux in the ocean, J. Geophys. Res., 87, 2071,

511 https://doi.org/10.1029/JC087iC03p02071, 1982.

512 McPhee, M. G., Ackley, S. F., Guest, P., Stanton, T. P., Huber, B. A., Martinson, D. G., Morison, J. H., Muench, R. D., and

513 Padman, L.: The Antarctic Zone Flux Experiment, Bull. Amer. Meteor. Soc., 77, 1221–1232, https://doi.org/10.1175/1520-

514 0477(1996)077<1221:TAZFE>2.0.CO;2, 1996.

515 McPhee, M. G., Kottmeier, C., and Morison, J. H.: Ocean Heat Flux in the Central Weddell Sea during Winter, J. Phys.

516 Oceanogr., 29, 1166–1179, https://doi.org/10.1175/1520-0485(1999)029<1166:OHFITC>2.0.CO;2, 1999.

517 McPhee, M. G., Morison, J. H., and Nilsen, F.: Revisiting heat and salt exchange at the ice-ocean interface: Ocean flux and

518 modeling considerations, J. Geophys. Res., 113, C06014, https://doi.org/10.1029/2007JC004383, 2008.

519 Miles, B. W. J., Stokes, C. R., and Jamieson, S. S. R.: Simultaneous disintegration of outlet glaciers in Porpoise Bay (Wilkes

520 Land), East Antarctica, driven by sea ice break-up, The Cryosphere, 11, 427–442, https://doi.org/10.5194/tc-11-427-2017,

521 2017.

522 Millero, F.: Freezing point of seawater, Eighth Report of the Joint Panel on Oceanographic Tables and Standards, 28, 29–31,

523 1978.

524 Millero, F. J. and Poisson, A.: International one-atmosphere equation of state of seawater, Deep Sea Research Part A.

525 Oceanographic Research Papers, 28, 625–629, https://doi.org/10.1016/0198-0149(81)90122-9, 1981.

526 Pan, H., Lv, X., Wang, Y., Matte, P., Chen, H., and Jin, G.: Exploration of Tidal-Fluvial Interaction in the Columbia River

527 Estuary Using S_TIDE, J. Geophys. Res. Oceans, 123, 6598–6619, https://doi.org/10.1029/2018JC014146, 2018.

528 Parkinson, C. L. and Washington, W. M.: A large-scale numerical model of sea ice, J. Geophys. Res., 84, 311,

529 https://doi.org/10.1029/JC084iC01p00311, 1979.

530 Perovich, D. K. and Elder, B.: Estimates of ocean heat flux at SHEBA: ESTIMATES OF OCEAN HEAT FLUX AT

531 SHEBA, Geophys. Res. Lett., 29, 58-1-58–4, https://doi.org/10.1029/2001GL014171, 2002.

532 Purdie, C. R., Langhorne, P. J., Leonard, G. H., and Haskell, T. G.: Growth of first-year landfast Antarctic sea ice

533 determined from winter temperature measurements, Ann. Glaciol., 44, 170–176,

534 https://doi.org/10.3189/172756406781811853, 2006.

535 Raphael, M. N. and Handcock, M. S.: A new record minimum for Antarctic sea ice, Nat Rev Earth Environ, 3, 215–216,

536 https://doi.org/10.1038/s43017-022-00281-0, 2022.

537 Screen, J. A. and Simmonds, I.: The central role of diminishing sea ice in recent Arctic temperature amplification, Nature,

538 464, 1334–1337, https://doi.org/10.1038/nature09051, 2010.

539 Semtner, A. J.: A Model for the Thermodynamic Growth of Sea Ice in Numerical Investigations of Climate, J. Phys.

540 Oceanogr., 6, 379–389, https://doi.org/10.1175/1520-0485(1976)006<0379:AMFTTG>2.0.CO;2, 1976.

541 Sirevaag, A.: Turbulent exchange coefficients for the ice/ocean interface in case of rapid melting, Geophys. Res. Lett., 36,

542 L04606, https://doi.org/10.1029/2008GL036587, 2009.

543 Untersteiner, N.: On the mass and heat budget of arctic sea ice, Arch. Met. Geoph. Biokl. A., 12, 151–182,

544 https://doi.org/10.1007/BF02247491, 1961.

545 Vihma, T.: Surface heat budget over the Weddell Sea: Buoy results and model comparisons, J. Geophys. Res., 107, 3013,

546 https://doi.org/10.1029/2000JC000372, 2002.

547 Wang, J., Luo, H., Yang, Q., Liu, J., Yu, L., Shi, Q., and Han, B.: An Unprecedented Record Low Antarctic Sea-ice Extent

548 during Austral Summer 2022, Adv. Atmos. Sci., s00376-022-2087–1, https://doi.org/10.1007/s00376-022-2087-1, 2022.

549 Yang, Y., Zhijun, L., Leppäranta, M., Cheng, B., Shi, L., and Lei, R.: Modelling the thickness of landfast sea ice in Prydz

550 Bay, East Antarctica, Antarctic Science, 28, 59–70, https://doi.org/10.1017/S0954102015000449, 2016.

551 Zhao, J., Yang, Q., Cheng, B., Leppäranta, M., Hui, F., Xie, S., Chen, M., Yu, Y., Tian, Z., Li, M., and Zhang, L.: Spatial

552 and temporal evolution of landfast ice near Zhongshan Station, East Antarctica, over an annual cycle in 2011/2012, Acta

553 Oceanol. Sin., 38, 51–61, https://doi.org/10.1007/s13131-018-1339-5, 2019.

554 Zhao, J., Cheng, B., Vihma, T., Heil, P., Hui, F., Shu, Q., Zhang, L., and Yang, Q.: Fast Ice Prediction System (FIPS) for

555 land-fast sea ice at Prydz Bay, East Antarctica: an operational service for CHINARE, Ann. Glaciol., 61, 271–283,

556 https://doi.org/10.1017/aog.2020.46, 2020.

557 Zhao, J., Yang, Q., Cheng, B., Wang N., Hui, F., Shen H., Han S., Zhang, L., and Timo Vihma,: Snow and land-fast sea ice

558 thickness derived from thermistor chain buoy in the Prydz Bay, Antarctic, Haiyang Xuebao, 115-127,

559 https://doi.org/10.3969/j.issn.0253-4193.2017.11.011, 2017 (in Chinese).

560